

# Large field-like torque in amorphous Ru<sub>2</sub>Sn<sub>3</sub> originated from the intrinsic spin Hall effect

Thomas J. Peterson<sup>§1</sup>, Mahendra DC<sup>§1</sup>, Yihong Fan<sup>2</sup>, Junyang Chen<sup>2</sup>, Delin Zhang<sup>2</sup>, Hongshi Li<sup>2</sup>, Przemyslaw Swatek,<sup>2</sup> Javier Garcia-Barriocanal<sup>3</sup>, Jian-Ping Wang<sup>1,2\*</sup>

<sup>1</sup> School of Physics and Astronomy, University of Minnesota, Minneapolis, Minnesota 55455, USA

<sup>2</sup> Electrical and Computer Engineering Department, University of Minnesota, Minneapolis, Minnesota 55455, USA

<sup>3</sup> Characterization Facility, University of Minnesota, 100 Union Street SE, Minneapolis, MN, 55455

\* Email: jpwang@umn.edu; corresponding author

§ Equal contribution authors

## Abstract

We investigated temperature dependent current driven spin-orbit torques in magnetron sputtered Ru<sub>2</sub>Sn<sub>3</sub> (4 and 10 nm) /Co<sub>20</sub>Fe<sub>60</sub>B<sub>20</sub> (5 nm) layered structures with in-plane magnetic anisotropy. The room temperature damping-like and field-like spin torque efficiencies of the amorphous Ru<sub>2</sub>Sn<sub>3</sub> films were extracted to be as large as  $0.14 \pm 0.008$  and  $-0.2 \pm 0.009$ , respectively, by utilizing the second harmonic Hall technique. The large field-like torque in the relatively thicker Ru<sub>2</sub>Sn<sub>3</sub> (10 nm) thin film is unique compared to the traditional spin Hall materials interfaced with thick magnetic layers with in-plane magnetic anisotropy which typically have negligible field-like torques. Additionally, the observed room temperature field-like torque efficiency in Ru<sub>2</sub>Sn<sub>3</sub> (10 nm)/CoFeB (5 nm) is up to three times larger than the damping-like torque ( $-0.20 \pm 0.009$  and  $0.07 \pm 0.012$ , respectively) and thirty times larger at 50 K ( $-0.29 \pm 0.014$  and  $0.009 \pm 0.017$ , respectively). The temperature dependence of the field-like torques are unique and show dominant contributions from the intrinsic spin Hall effect with intrinsic spin conductivity up to  $-240 \pm 19$

$\hbar/2e (\Omega\text{cm})^{-1}$  while the damping-like torques show dominate contributions from the extrinsic spin Hall effects with sum of the skew scattering and side jump up to  $-175 \pm 19 \hbar/2e (\Omega\text{cm})^{-1}$ . Through macro-spin calculations, we found that including field-like torques on the order or larger than the damping-like torque can reduce the switching critical current and the switching time for a perpendicular ferromagnetic layer.

## Introduction

Devices designed with spin orbit torque (SOT) materials have been considerably studied as candidates for developing ultrafast-speed and ultralow-energy spin memory and logic applications, such as SOT magnetic random access memory (SOT-MRAM)<sup>1–3</sup>. The most commonly studied SOT generators are heavy metals (HMs), such as Ta<sup>1,4,5</sup>, W<sup>6–8</sup>, Pt<sup>9–11</sup>, and topological insulators (TIs), such as Bi<sub>2</sub>Se<sub>3</sub><sup>12–18</sup>, (Bi<sub>x</sub>Sb<sub>y</sub>)<sub>2</sub>Te<sub>3</sub><sup>19,20</sup>, Bi<sub>2</sub>Te<sub>3</sub><sup>19</sup>. HMs with low resistivities (10-300  $\mu\Omega\text{cm}$ <sup>1,4–11</sup>) have charge-to-spin and spin-to-charge conversion efficiencies ( $\zeta_S$ ) generated primarily by the bulk spin Hall effect, and have spin torque efficiency in the range of 0.01-0.5.<sup>1,4–11</sup> However, TI materials with larger resistivities (1000-100,000  $\mu\Omega\text{cm}$ <sup>12–20</sup>) can have  $\zeta_S$  much larger than 1. The efficient spin torque generation in TIs is due to spin polarized surface states where the electron's spin is perpendicularly locked with its momentum.<sup>12,14,21–23</sup> In addition to the spin-momentum locking, the bulk spin Hall effect<sup>1,24</sup> and the interfacial Rashba effect<sup>9,25,26</sup> can also generate spin torques in TI materials. The spin density generation in TIs has been shown to improve in nano-crystalline systems, sputtered Bi<sub>2</sub>Se<sub>3</sub> has shown larger spin torque efficiencies (10-1000x) compared to single crystal molecular beam epitaxy grown Bi<sub>2</sub>Se<sub>3</sub> due to quantum confinement from the grain size reduction in dimensionality.<sup>15,17</sup>

However, for SOT-MRAM applications the typical metallic free layers can have current shunting due to the high resistivity of the TI SOT channel, increasing the critical current required for magnetization switching. Novel lower resistivity topological materials are required to reduce the critical switching current density.<sup>27</sup> A possible new material is the Ru<sub>2</sub>Sn<sub>3</sub> system. Ru<sub>2</sub>Sn<sub>3</sub> is a low resistivity TI material, with a resistivity ranging from 800-2000  $\mu\Omega\text{cm}$  (10x lower than sputtered Bi<sub>2</sub>Se<sub>3</sub>). The Ru<sub>2</sub>Sn<sub>3</sub> band structure is a semiconductor at room temperature. Due to a crystalline phase change that occurs at 160 K, the band structure of the low temperature phase is a

TI with highly anisotropic surface states.<sup>28</sup> The TI surface states in the low temperature phase have been observed via angle resolved photoemission spectroscopy (ARPES) experiments.<sup>28</sup> The phase change is accompanied by a characteristic peak in resistivity centered at 160 K.<sup>29,30</sup> The low temperature crystal phase has been experimentally shown to stabilize at room temperature via applied pressure.<sup>31</sup> The Ru<sub>2</sub>Sn<sub>3</sub> crystalline structure is also robust against annealing and stable up to 1100°C, making it a possible candidate for industrial application and CMOS integration.<sup>32</sup>

In this manuscript, we report large field-like torques with non-negligible damping-like torques in sputtered, amorphous Ru<sub>2</sub>Sn<sub>3</sub> thin films. We confirm the amorphous structure of the films with high resolution tunneling electron microscopy and the 2:3 composition with Rutherford backscattering techniques. Through the second harmonic Hall measurement we can extract and characterize the damping-like (DL) and field-like (FL) SOTs originating in the Ru<sub>2</sub>Sn<sub>3</sub> films. We find room temperature a  $\zeta_S^{DL}$  of  $0.14 \pm 0.008$  and  $0.07 \pm 0.012$  and a  $\zeta_S^{FL}$  of  $-0.03 \pm 0.006$  and  $-0.20 \pm 0.009$  for 4 and 10 nm Ru<sub>2</sub>Sn<sub>3</sub> films, respectively. By analyzing the resistivity dependence of the spin torque efficiencies, we extracted the contributions from the intrinsic and extrinsic spin Hall effects. The FL torques show dominant contributions from the intrinsic spin Hall effect with intrinsic spin conductivity up to  $-240 \pm 19 \hbar/2e (\Omega\text{cm})^{-1}$  while the DL torques show dominate contributions from the extrinsic spin hall effects with sum of the skew scattering and side jump up to  $-175 \pm 19 \hbar/2e (\Omega\text{cm})^{-1}$ . We performed macro-spin calculations of the Landau-Lifshitz-Gilbert (LLG) equation to simulate switching a perpendicular magnetic layer including both the DL and FL torques generated from our Ru<sub>2</sub>Sn<sub>3</sub> SOT channel. We find the inclusion of FL torques three times greater than the DL can reduce the critical current required for switching and the switching time by almost 50% compared to the DL torque only case.

## Materials Growth and Characterization

To investigate the SOTs in  $\text{Ru}_2\text{Sn}_3$ , thin films of  $\text{Ru}_2\text{Sn}_3$ (4 nm, 10 nm)/ $\text{Co}_{20}\text{Fe}_{60}\text{B}_{20}$ (5 nm)/ $\text{MgO}$ (2 nm)/ $\text{Ta}$ (2 nm) were deposited using magnetron sputtering on 300 nm thermally oxidized Si substrates, with a base pressure of  $9 \times 10^{-8}$  Torr and an Ar working pressure of 1.5 mTorr. The 4 and 10 nm  $\text{Ru}_2\text{Sn}_3$  samples are labeled as RS4 and RS10, respectively. The  $\text{Ru}_2\text{Sn}_3$  thin films were sputtered with a pure  $\text{Ru}_2\text{Sn}_3$  alloy target but due to the non-empirical nature of magnetron sputtering, the composition may slightly drift from the optimal value. To confirm the ratio of Ru to Sn, the composition has been measured using Rutherford back scattering (RBS), with a  $\text{He}^+$  beam with maximum energy of 4.7 MeV and current of 40  $\mu\text{C}$ , on a bare 17 nm  $\text{Ru}_2\text{Sn}_3$  thin film, as shown in supplemental Figure 3 (a). The final elemental composition is calculated from fitting the simulation results done in QUARK to the measured RBS data. The final composition of the sputtered  $\text{Ru}_2\text{Sn}_3$  is calculated to be 40.2 and 59.8% ( $\pm 0.15\%$ ), respectively. Additionally, tunneling electron microscope (TEM) measurements were done on the RS4 and 10 samples and show an amorphous phase of the  $\text{Ru}_2\text{Sn}_3$ . The bright-field TEM and High-Angle Annular Dark-Field (HAADF) images of RS10 shown in Figure 1 (a,b) suggests that no crystalline structure is observed in the  $\text{Ru}_2\text{Sn}_3$  layer with small crystallites in the  $\text{Co}_{20}\text{Fe}_{60}\text{B}_{20}$  and  $\text{MgO}$  layers. Further investigation including selected area diffraction did not reveal any long-range order in the  $\text{Ru}_2\text{Sn}_3$  layer, indicating this layer is amorphous throughout, as shown in Figure 1 (c). Further

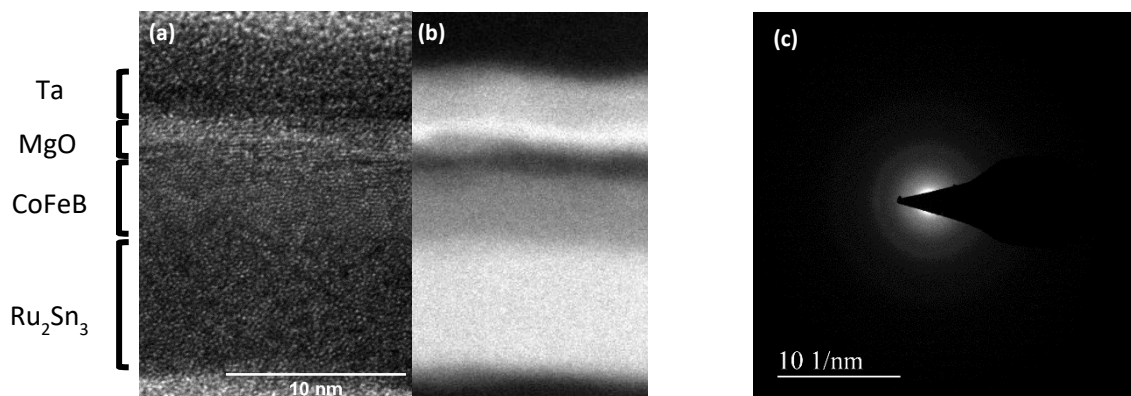


Figure 1. (a) Bright field transmission electron microscope image of the RS10 sample. (c) Selected area diffraction pattern of the RS10 sample. The diffuse ring seen suggests an amorphous film with no long-range order.

measurements of XRD and Raman spectroscopy on 17 nm Ru<sub>2</sub>Sn<sub>3</sub> thin films showed no indication of crystal structure, however, both measurements are limited by the film thickness.

### Second Harmonic Hall measurement for SOT characterization

To calculate the charge to spin conversion efficiency of the DL and FL torque contributions independently we utilize the harmonic Hall measurement technique.<sup>33–36</sup> The RS4 and RS10 samples were patterned into Hall bars with a length of 85  $\mu\text{m}$  and a width of 10  $\mu\text{m}$ . An AC current with frequency 133 Hz and peak value of 4 mA is applied through the channel. Figure 2 (a) shows a schematic of the second harmonic measurement. The Hall bar is rotated in the xy plane from 0 to 360 degrees, while the first and second harmonic Hall voltages are measured via two lock in amplifiers. Figure 2 (b) shows the resulting first harmonic Hall voltage which provides the planar Hall resistance and can be fitted by:

$$V_{xy}^{\omega} = R_{PHE} \sin 2\varphi I, \quad (1)$$

where  $\varphi$  is the in-plane angle.  $R_{PHE}$  is the planar Hall resistance. Figure 2 (c) shows the second harmonic Hall voltages and is given by,

$$\begin{aligned} V_{xy}^{2\omega} &= [V_{DL} \cos \varphi - V_{FL} (\cos 2\varphi \cos \varphi)] I \\ V_{DL} &= \frac{1}{2} R_{AHE} \frac{-H_{DL}}{H_{ext} + H_k} + I \propto \nabla T; \\ V_{FL} &= R_{PHE} \frac{H_{FL} + H_{Oe}}{H_{ext}}, \end{aligned} \quad (2)$$

where  $H_{ext}$  is the applied external field,  $H_k$  is the perpendicular anisotropy field, and  $I \propto \nabla T$  is the field independent thermal contributions arising from the anomalous Nernst and Seebeck effects.<sup>34</sup>  $H_{Oe}$  is the Oersted field resulting from the current in the RS layer.  $H_{Oe}$  is calculated to be roughly 0.12 and 0.43 Oe for the RS4 and RS10 samples, respectively. The extracted value of  $H_{FL}$  is about 5x larger than calculated value of  $H_{Oe}$ , suggesting the FL term is dominant over the Oersted contributions. There is a phase shift of roughly 90 degrees between the current direction and the

field direction from sample mounting.  $R_{\text{AHE}}$  is the anomalous Hall resistance and can be extracted by sweeping an out of plane field to 3 T and is measured down to 50K. The extracted 300K  $R_{\text{AHE}}$  values are 9.5 and 7.9  $\Omega$  for the RS4 and 10 samples respectively. The  $V_{\text{DL}}$  and  $V_{\text{FL}}$  voltages are extracted via fitting the second harmonic signals at various  $H_{\text{ext}}$  from 0.15-3 T shown in supplemental Figure 1 (a,b) at various sample temperatures from 50-300 K.  $V_{\text{DL}}$  is fitted to a linear relation to separate the field independent thermal contributions from the DL-SOT. The thermal term is the dominant contribution to  $V_{\text{DL}}$  in our samples ranging from 22 - 26  $\mu\text{V}$  and 14 -18  $\mu\text{V}$  for the RS4 and RS10 samples, respectively.  $H_{\text{DL}}$  and  $H_{\text{FL}}$  are the effective fields generated from the spin currents originating in the RS layer, and have the form:

$$H_{\text{DL}} = \frac{\hbar \zeta_{\text{DL}} J_{\text{RuSn}}}{2e M_S t_{\text{CoFeB}}} (\hat{\sigma} \times \hat{m}),$$

$$H_{\text{FL}} = \frac{\hbar \zeta_{\text{FL}} J_{\text{RuSn}}}{2e M_S t_{\text{CoFeB}}} [\hat{m} \times (\hat{\sigma} \times \hat{m})], \quad (3)$$

Where  $\hat{\sigma}$  and  $\hat{m}$  are the directions of the spin polarization and magnetization, respectively.  $M_S$  is the saturation magnetization of the CoFeB layer and is measured via vibrating sample magnetometry down to 50K, shown in supplemental Figure 3, the room temperature value of  $M_S$

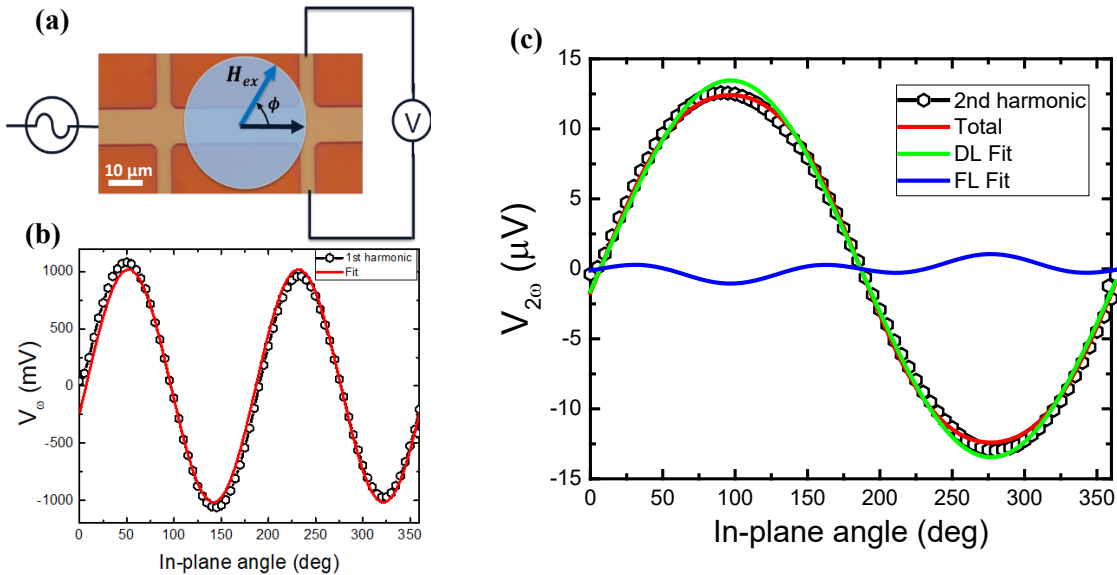


Figure 2. (a) Diagram of the harmonic Hall measurement, a Hall bar with a length of 85  $\mu\text{m}$  and a width of 10  $\mu\text{m}$  is rotated bar is rotated in the xy plane from 0 to 360 degrees, while the first and second harmonic Hall voltages are measured via two lock in amplifiers. (b) The first harmonic and (c) second Hall voltages for the RS10 sample rotated in a 1500 Oe external field at 300 K fitted to Equations 1 and 2, respectively.

is 1100 emu/cc.  $t_{CoFeB}$  is the thickness of the CoFeB layer and  $J_{RuSn}$  is the estimated charge current flowing in the RS channel assuming parallel resistors.  $\zeta_{DL}$  and  $\zeta_{FL}$  are the effective charge to spin conversion efficiency for DL and FL torques, respectively. We depict the fitted values of  $\zeta_{DL}$  and  $\zeta_{FL}$ , as a function of temperature in Figure 3 (a,b).

Although both types of torque exhibit nearly linear dependence on temperature, they follow opposite trends, i.e., the magnitude DL torque increases with increasing temperature, whereas the magnitude of the FL torque decreases with increasing temperature. The opposite behavior of DL and FL torques suggests the torques are originating from separate effects. The resistivity of the RS and CoFeB layers were estimated assuming a parallel circuit model, assuming the resistivity of the RS4 and 10 are the same, shown in Figure 3 (c). The resistivity of the RS layer linearly increases with a decrease in temperature, without the characteristic peak in resistivity expected from the phase transformation expected at 160 K, indicating there was no crystalline transition into the TI phase. The temperature vs. resistivity observed suggests our films remained amorphous, however we still see large spin torques generated by the RS thin film, indicating the presence of large SOC. The extracted  $\zeta_{DL}$  and  $\zeta_{FL}$  also do not increase sharply below 160 K, which would be expected if the system transitioned into the TI phase due to the emergence of spin polarized topological surface states.

Figure 3 (d) shows the extracted spin torque efficiencies of the RS10 sample as a function of the RS layer resistivity. The FL torque increases in magnitude from the low resistivity room temperature measurement to a higher value in the high resistivity low temperature measurement. However, the DL torques follow an opposite trend with resistivity suggesting the torques are arising from separate effects.



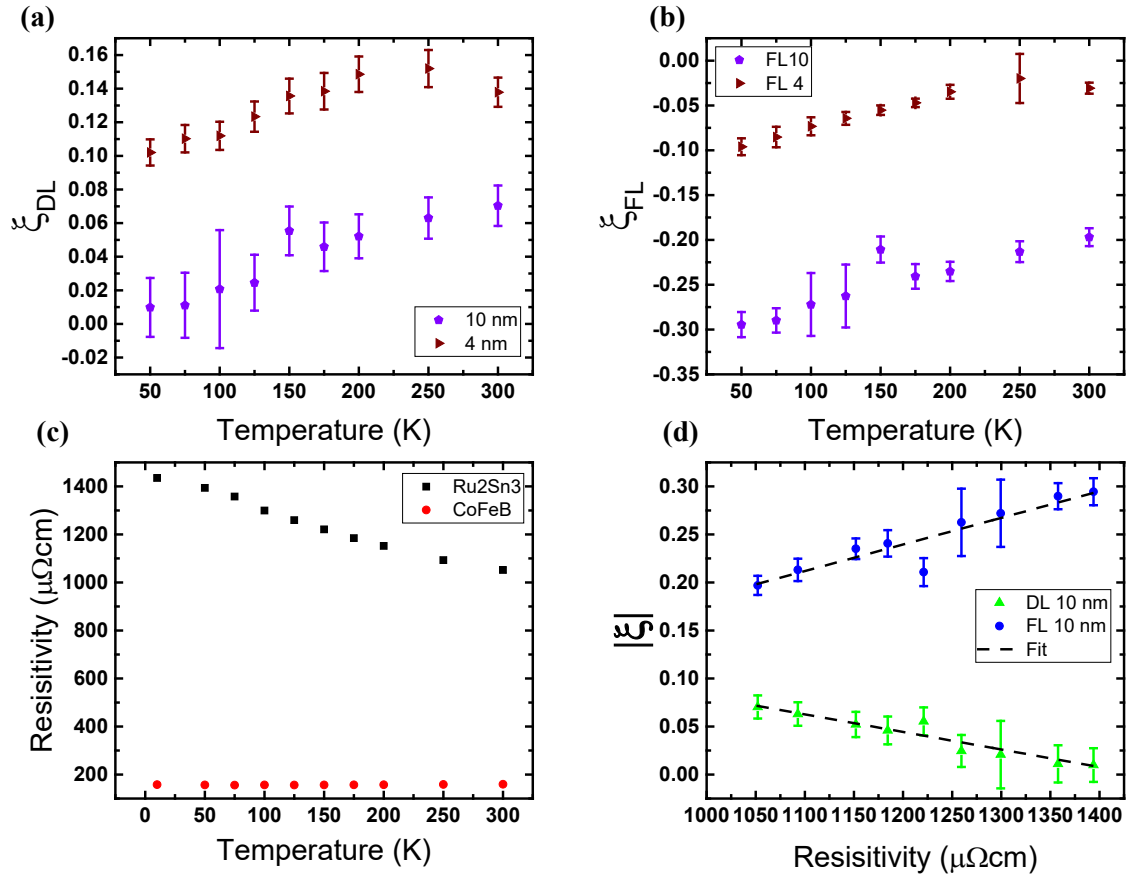


Figure 3. (a) Temperature dependence of the efficiency of the SOT induced by damping-like torque and (b) field-like torque. (c) Temperature dependent resistivities for the CoFeB and RS bilayers estimated from the channel resistance assuming a parallel resistor. The resistivity is assumed to be constant with film thickness (d) Relation between magnitude  $\zeta_{DL,FL}$  and the resistivity of the RS10 sample. Dashed line shows the fit to Equation 4.

The temperature dependent torque efficiencies can be analyzed by using following equation<sup>37,38</sup>

$$-\zeta = \sigma_s^{Int} \rho + \frac{\sigma_s^{SJ} \rho_0^2 + \alpha_{ss} \rho_0}{\rho}, \quad (4)$$

where  $\rho$ ,  $\rho_0$ ,  $\sigma_s^{Int}$ ,  $\sigma_s^{SJ}$ , and  $\alpha_{ss}$  are longitudinal resistivity, residual resistivity (resistivity at 0 K), intrinsic spin conductivity, spin conductivity due to the side jump, and skew scattering angle, respectively. The residual resistivity of  $1450 \mu\Omega\text{cm}$  is extracted from the  $\text{Ru}_2\text{Sn}_3$  resistivity vs temperature trend in Figure 3 (c). As shown in Figure 3 (d),  $\zeta_{FL}$  increases monotonically with  $\rho$  indicating that the FLT is originated from the intrinsic spin Hall effect.  $\zeta_{FL}$  is larger in the RS10 compared to the RS4 sample which agrees with the intrinsic spin Hall effect mechanism.  $\zeta_{DL}$

	$\zeta$	$\sigma_s^{Int} (\Omega cm)^{-1}$	$\sigma_s^{SJ} \rho_0^2 + \alpha_{ss} \rho_0 (\mu \Omega cm)$
RS4	DL	$73 \pm 11$	$-157 \pm 16$
RS4	FL	$240 \pm 19$	$-57 \pm 27$
RS10	DL	$13 \pm 12$	$-175 \pm 19$
RS10	FL	$117 \pm 10$	$-106 \pm 15$

Table I. Extracted intrinsic spin conductivity and extrinsic spin Hall components from the side jump and skew scattering from fitting equation 4 to the DL and FL spin torques for the RS4, 10 samples.

decreases with increase in  $\rho$  against the belief of intrinsic spin Hall effect. By fitting Eqn. 4 over the data the estimated parameters are shown in Table I. For both RS4 and RS10 the FL torque efficiencies show larger  $\sigma_s^{Int}$  than their DL counterparts suggesting the FL torques are mainly originating from the intrinsic spin Hall effect. Similarly the FL torques have smaller  $\sigma_s^{SJ} \rho_0^2 + \alpha_{ss} \rho_0$  extrinsic parameters than the DL torques, suggesting the DL torques are originating from the extrinsic spin hall effects.

Additionally, considering the scenario of an interfacial Rashba torque, this increase in FL torque efficiency could be due to the increase of bulk resistivity, increasing the current flowing through the interface increasing the FL torques. The decreased current through the bulk of the RS layer would decrease the current generated via the SHE reducing the DL torque efficiency. A similar resistivity dependence of the FL torque was observed in Ta systems.<sup>39-41</sup>

The dominant FL torque term with non-negligible DL torque seen in the RS10 sample is a unique result. Typically, HM systems with large SOC such as Pt, W, and Ta interfaced with thick magnetic layers with in-plane magnetic anisotropy are dominated by the SHE, generating a large DL and negligible FL term.<sup>34</sup> In the case of Ta, non-negligible FL torques have been observed,<sup>34,39,40</sup> however, the DL torque typically remains the dominant torque. In the case of HM systems interfaced with thin magnetic layers with out of plane magnetic anisotropy FL can be comparable or larger than the DL torque.<sup>4,39,42</sup> Additionally, inserting a Hf spacer between W and a ferromagnet has been shown to increase the FL torque to be above the DL torque.<sup>43</sup> However, the FL torques in

our RS films has very different temperature dependence than the Ta and W/Hf devices. In those samples the field-like torque has a very strong temperature dependence, decreasing almost to zero and even changing sign of the FL torque at low temperatures while the damping-like torque is almost temperature independent.<sup>39</sup> Large FL torques have been observed in two-dimensional materials such as MoS<sub>2</sub> and WSe<sub>2</sub> due a strong Rashba-Edelstein effect; however, the DL torques in the monolayer systems are negligible since no bulk effects can contribute.<sup>44</sup>

### Macro-Spin Simulations

Often when studying the switching dynamics in SOT-based MTJs the focus is on the DL torque with the FL torque neglected. To study the SOT switching of a PMA layer considering large FL torques on the order or larger than the DL term, we performed macro-spin approximation

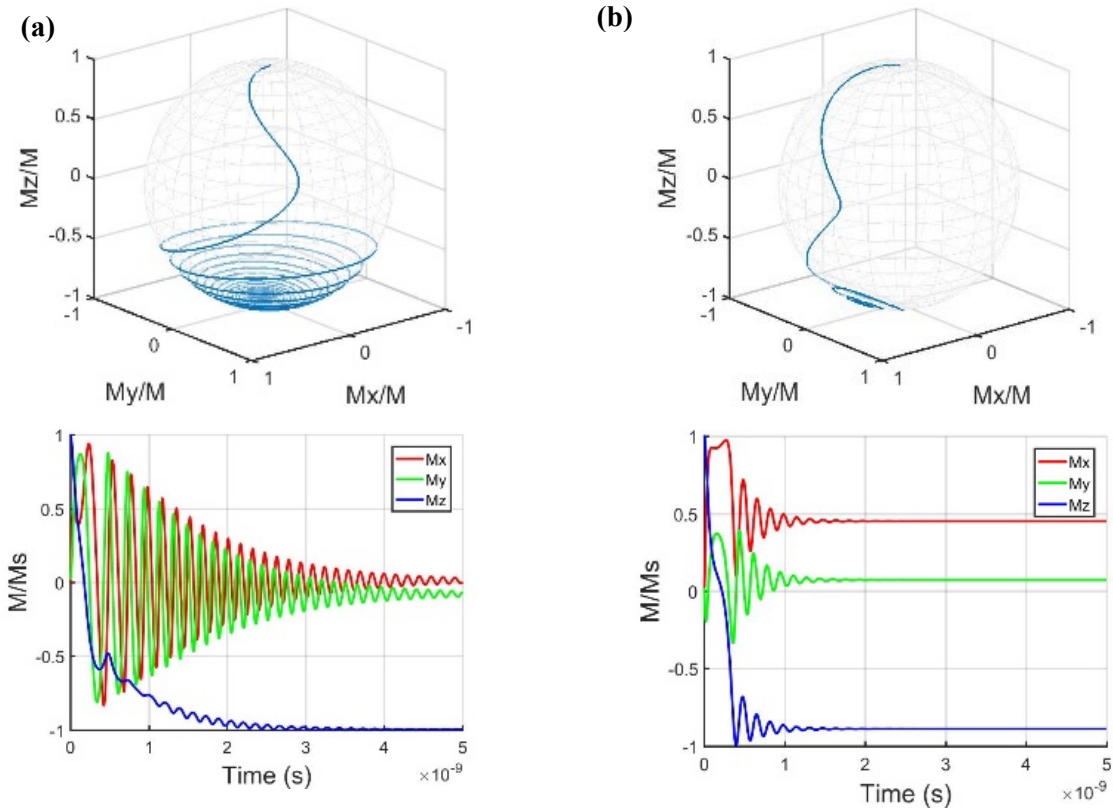


Figure 4. Above. Time evolutions of the magnetization direction of the FM layer subject to an x direction external field of 500 Oe projected on a unit sphere. Below. The Cartesian projections of FM magnetization direction as a function of time. Calculations done for (a)  $\zeta_{DL}$  of 0.06 and  $\zeta_{FL}$  of 0, (b)  $\zeta_{DL}$  of 0.06 and  $\zeta_{FL}$  of 0.18.

calculations. The following LLG equation is numerically solved to determine the dynamics of the PMA layer subject to a spin current generated by a SOT channel:

$$(1 + \alpha^2) \frac{d\hat{m}}{dt} = -\gamma \hat{m} \times H_{eff} + \alpha \hat{m} \times \frac{d\hat{m}}{dt} - H_{DL} \hat{m} \times (\hat{m} \times \hat{\sigma}) - H_{FL} (\hat{m} \times \hat{\sigma}), \quad (5)$$

where  $H_{eff}$  denotes the effective field, including the anisotropy field, demagnetization field, and external bias field,  $\gamma$  is the gyromagnetic ratio,  $\alpha$  is the Gilbert damping factor, and  $\sigma$  is the electron polarization direction of the spin polarized current arising from the SOT channel. For the calculations, we assume a 1nm FM layer with a perpendicular magnetic anisotropy field of 1.5 T,  $M_s$  value of 1000 emu/cc, and a damping constant of 0.02. We apply a  $H_{ext}$  of 500 Oe in the  $\hat{x}$  direction to break the symmetry allowing for switching. We calculate the time evolution of the magnetization as it is subject to the DL and FL torques arising from the SOT channel at a critical current density for switching. We assume five cases with a fixed  $\zeta_{DL}$  of 0.06 and a varied  $\zeta_{FL}$  of 0, 0.06, 0.12, 0.18, and 0.24. The resulting FM magnetization dynamics and projections for the  $\zeta_{FL}$  of 0 and 0.18 are shown in Figure 6. For each case, the current in the SOT channel is varied until a minimum critical current for switching is reached, we define this value as  $J_c$  in Table II. Current is applied during the entire simulation. The switching time is defined as the time at which the  $M_z$  projection damps to a stable minimum value near  $M_z = -1$ .

The five simulated cases show a clear trend of  $J_c$  with the ratio of FL to DL spin torques strengths. As the FL torques increases we see a reduction of  $J_c$  from  $35 \times 10^{11} \text{A/m}^2$  for the

$\zeta_{FL}/\zeta_{DL}$	$\zeta_{FL}$	$\zeta_{DL}$	$J_c \left( 10^{11} \frac{\text{A}}{\text{m}^2} \right)$	$t_{switch} \text{ (ns)}$
0	0	0.06	35	3
1	0.06	0.06	32	1.5
2	0.12	0.06	25	1.5
3	0.18	0.06	18.5	1.5
4	0.24	0.06	14.5	1.5

Table II. Simulation variables for switching a 1 nm PMA layer with different contributions from the damping-like and field-like spin torques. The current is varied until a minimum critical current for switching is reached. The switching time is defined as the time at which the  $M_z$  projection reaches a stable minimum value.

$\zeta_{FL}/\zeta_{DL} = 0$  case to  $14 \times 10^{11} \text{A/m}^2$  for the  $\zeta_{FL}/\zeta_{DL} = 4$  case. We also observe a reduction of the switching time for all cases with nonzero FL torques. However, as the strength of the FL torque increases, we also see an increase of the stabilization value of  $M_z$  as it drifts away from the fully switched  $-1\hat{z}$  value. The results seen here are macro-spin and neglect any effects due to magnetic domains within the FM material. Recent micro-spin model calculations done by Zuwei et al. on in-plane MTJ stacks with a varied FL torque strength, show similar results as seen here.<sup>45</sup> Their simulations similarly showed a reduction of  $J_c$  and switching time due to the FL torque decreasing the time for domains to nucleate in the material. It is likely that  $J_c$  and switching seen in our macro-spin calculations would be further reduced due to domain effects within the FM material. Analytic expressions for the SOT critical current considering both FL and DL torques have been derived Zhu et al.<sup>46</sup> These formulas agree with the numerical simulations and show a reduction of critical current through the large FL torques. Additionally, conditions for stable magnetization switching after removing SOT currents were found showing FL torques are a viable for p-MTJ switching.

## Conclusions

Current driven SOTs in magnetron sputtered  $\text{Ru}_2\text{Sn}_3/\text{Co}_{20}\text{Fe}_{60}\text{B}_{20}$  layered structures with in-plane magnetization were investigated. We extracted the DL and FL spin torque efficiencies of the RS4 and RS10 samples utilizing the harmonic Hall technique. The calculated room temperature DL torque and FL torque for the RS4(RS10) system are  $0.14 \pm 0.008$  ( $0.07 \pm 0.012$ ) and  $-0.03 \pm 0.006$  ( $-0.20 \pm 0.009$ ), respectively. The opposite trend of the DL and FL torques with temperature and resistivity suggest the torques are arising from separate effects. The FL torques show dominant contributions from the intrinsic SHE with intrinsic spin conductivity up to  $-240 \pm 19 \hbar/2e$  ( $\Omega\text{cm}$ )<sup>-1</sup> while the DL torques show dominate contributions from the extrinsic SHE with sum of the skew scattering and side jump up to  $-175 \pm 19 \hbar/2e$  ( $\Omega\text{cm}$ )<sup>-1</sup>. The trend of the torque efficiencies with

temperature suggests the FL torque could also be arising from interfacial effects. We performed macro-spin calculations of switching a PMA FM layer including contributions from both the DL and FL torques. The simulations suggest that including FL torques on the order or larger than the DL torque reduces  $J_c$  and the switching time.

### **Acknowledgements**

This work was supported in part by ASCENT, one of six centers in JUMP, a Semiconductor Research Corporation (SRC) program sponsored by DARPA. This material is based upon work supported in part by the National Science Foundation under the Scalable Parallelism in the Extreme (SPX) Grant. The TEM was performed by Dr. Jason Myers and the RBS was performed by Dr. Greg Haugstad in the College of Science and Engineering (CSE) Characterization Facility at the University of Minnesota (UMN), supported in part by the NSF through the UMN MRSEC program. Portions of this work were conducted in the Minnesota Nano Center, which is supported by the National Science Foundation through the National Nano Coordinated Infrastructure Network (NNCI) under Award Number ECCS-2025124.

### **References**

- <sup>1</sup> L. Liu, C.F. Pai, Y. Li, H.W. Tseng, D.C. Ralph, and R.A. Buhrman, *Science* (80-. ). **336**, 555 (2012).
- <sup>2</sup> S. Manipatruni, D.E. Nikonov, and I.A. Young, *Appl. Phys. Express* **7**, 103001 (2014).
- <sup>3</sup> M. Wang, Y. Zhang, X. Zhao, and W. Zhao, *Micromachines* **6**, 1023 (2015).
- <sup>4</sup> J. Kim, J. Sinha, M. Hayashi, M. Yamanouchi, S. Fukami, T. Suzuki, S. Mitani, and H. Ohno, *Nat. Mater.* **12**, 240 (2013).
- <sup>5</sup> Z. Zhao, M. Jamali, A.K. Smith, and J.P. Wang, *Appl. Phys. Lett.* **106**, 132404 (2015).
- <sup>6</sup> Q. Hao, W. Chen, and G. Xiao, *Appl. Phys. Lett.* **106**, 182403 (2015).
- <sup>7</sup> C.F. Pai, L. Liu, Y. Li, H.W. Tseng, D.C. Ralph, and R.A. Buhrman, *Appl. Phys. Lett.* **101**, 122404 (2012).

- <sup>8</sup> T.J. Peterson, P. Sahu, D. Zhang, M. D.C., and J.-P. Wang, IEEE Trans. Magn. **55**, 1 (2019).
- <sup>9</sup> I.M. Miron, K. Garello, G. Gaudin, P.J. Zermatten, M. V. Costache, S. Auffret, S. Bandiera, B. Rodmacq, A. Schuhl, and P. Gambardella, Nature **476**, 189 (2011).
- <sup>10</sup> L. Liu, O.J. Lee, T.J. Gudmundsen, D.C. Ralph, and R.A. Buhrman, Phys. Rev. Lett. **109**, 096602 (2012).
- <sup>11</sup> C.F. Pai, Y. Ou, L.H. Vilela-Leão, D.C. Ralph, and R.A. Buhrman, Phys. Rev. B - Condens. Matter Mater. Phys. **92**, 064426 (2015).
- <sup>12</sup> A.R. Mellnik, J.S. Lee, A. Richardella, J.L. Grab, P.J. Mintun, M.H. Fischer, A. Vaezi, A. Manchon, E.A. Kim, N. Samarth, and D.C. Ralph, Nature **511**, 449 (2014).
- <sup>13</sup> Y. Wang, P. Deorani, K. Banerjee, N. Koirala, M. Brahlek, S. Oh, and H. Yang, Phys. Rev. Lett. **114**, 257202 (2015).
- <sup>14</sup> M. Jamali, J.S. Lee, J.S. Jeong, F. Mahfouzi, Y. Lv, Z. Zhao, B.K. Nikolić, K.A. Mkhoyan, N. Samarth, and J.P. Wang, Nano Lett. **15**, 7126 (2015).
- <sup>15</sup> M. DC, R. Grassi, J.Y. Chen, M. Jamali, D. Reifsnyder Hickey, D. Zhang, Z. Zhao, H. Li, P. Quarterman, Y. Lv, M. Li, A. Manchon, K.A. Mkhoyan, T. Low, and J.P. Wang, Nat. Mater. **17**, 800 (2018).
- <sup>16</sup> M. DC, T. Liu, J.Y. Chen, T. Peterson, P. Sahu, H. Li, Z. Zhao, M. Wu, and J.P. Wang, Appl. Phys. Lett. **114**, 102401 (2019).
- <sup>17</sup> R. Ramaswamy, T. Dutta, S. Liang, G. Yang, M.S.M. Saifullah, and H. Yang, J. Phys. D. Appl. Phys. **52**, 224001 (2019).
- <sup>18</sup> M. DC, J.-Y. Chen, T. Peterson, P. Sahu, B. Ma, N. Mousavi, R. Harjani, and J.-P. Wang, Nano Lett. **19**, 4836 (2019).
- <sup>19</sup> K. Kondou, R. Yoshimi, A. Tsukazaki, Y. Fukuma, J. Matsuno, K.S. Takahashi, M. Kawasaki, Y. Tokura, and Y. Otani, Nat. Phys. **12**, 1027 (2016).
- <sup>20</sup> Y. Fan, P. Upadhyaya, X. Kou, M. Lang, S. Takei, Z. Wang, J. Tang, L. He, L. Te Chang, M. Montazeri, G. Yu, W. Jiang, T. Nie, R.N. Schwartz, Y. Tserkovnyak, and K.L. Wang, Nat. Mater. **13**, 699

(2014).

<sup>21</sup> M.Z. Hasan and C.L. Kane, Rev. Mod. Phys. **82**, 3045 (2010).

<sup>22</sup> Y. Ando, T. Hamasaki, T. Kurokawa, K. Ichiba, F. Yang, M. Novak, S. Sasaki, K. Segawa, Y. Ando, and M. Shiraishi, Nano Lett. **14**, 6226 (2014).

<sup>23</sup> C.H. Li, O.M.J. Van't Erve, J.T. Robinson, Y. Liu, L. Li, and B.T. Jonker, Nat. Nanotechnol. **9**, 218 (2014).

<sup>24</sup> A. Manchon and S. Zhang, Phys. Rev. B - Condens. Matter Mater. Phys. **79**, 094422 (2009).

<sup>25</sup> T. Suzuki, S. Fukami, N. Ishiwata, M. Yamanouchi, S. Ikeda, N. Kasai, and H. Ohno, Appl. Phys. Lett. **98**, 142505 (2011).

<sup>26</sup> A. Manchon, H.C. Koo, J. Nitta, S.M. Frolov, and R.A. Duine, Nat. Mater. **14**, 871 (2015).

<sup>27</sup> A.S. Everhardt, M. DC, X. Huang, S. Sayed, T.A. Gosavi, Y. Tang, C.C. Lin, S. Manipatruni, I.A. Young, S. Datta, J.P. Wang, and R. Ramesh, Phys. Rev. Mater. **3**, 051201 (2019).

<sup>28</sup> Q.D. Gibson, D. Evtushinsky, A.N. Yaresko, V.B. Zabolotnyy, M.N. Ali, M.K. Fuccillo, J. Van Den Brink, B. Büchner, R.J. Cava, and S. V. Borisenko, Sci. Rep. **4**, 1 (2014).

<sup>29</sup> D.J. Poutcharovsky, K. Yvon, and E. Parthé, J. Less-Common Met. **40**, 139 (1975).

<sup>30</sup> Y. Shiomi and E. Saitoh, AIP Adv. **7**, 1 (2017).

<sup>31</sup> S. Zhang, Q.D. Gibson, W. Yi, J. Guo, Z. Wang, Y. Zhou, H. Wang, S. Cai, K. Yang, A. Li, Q. Wu, R.J. Cava, L. Sun, and Z. Zhao, Epl **117**, (2017).

<sup>32</sup> T.B. Massalski and H. (Hiroaki) Okamoto, *Binary Alloy Phase Diagrams* (ASM International, 2018).

<sup>33</sup> M. Kawaguchi, K. Shimamura, S. Fukami, F. Matsukura, H. Ohno, T. Moriyama, D. Chiba, and T. Ono, Appl. Phys. Express **6**, 113002 (2013).

<sup>34</sup> C.O. Avci, K. Garelo, M. Gabureac, A. Ghosh, A. Fuhrer, S.F. Alvarado, and P. Gambardella, Phys. Rev. B - Condens. Matter Mater. Phys. **90**, 224427 (2014).

<sup>35</sup> M. Hayashi, J. Kim, M. Yamanouchi, and H. Ohno, Phys. Rev. B - Condens. Matter Mater. Phys. **89**, 144425 (2014).

<sup>36</sup> Y. Wen, J. Wu, P. Li, Q. Zhang, Y. Zhao, A. Manchon, J.Q. Xiao, and X. Zhang, Phys. Rev. B **95**,



104403 (2017).

<sup>37</sup> Y. Tian, L. Ye, and X. Jin, Phys. Rev. Lett. **103**, 087206 (2009).

<sup>38</sup> E. Sagasta, Y. Omori, S. Vélez, R. Llopis, C. Tollan, A. Chuvilin, L.E. Hueso, M. Gradhand, Y. Otani, and F. Casanova, Phys. Rev. B **98**, 060410 (2018).

<sup>39</sup> J. Kim, J. Sinha, S. Mitani, M. Hayashi, S. Takahashi, S. Maekawa, M. Yamanouchi, and H. Ohno, Phys. Rev. B - Condens. Matter Mater. Phys. **89**, 174424 (2014).

<sup>40</sup> X. Qiu, Z. Shi, W. Fan, S. Zhou, and H. Yang, Adv. Mater. **30**, 1705699 (2018).

<sup>41</sup> M. Cecot, Ł. Karwacki, W. Skowroński, J. Kanak, J. Wrona, A. Zywczyk, L. Yao, S. Dijken, J. Barnaś, and T. Stobiecki, Sci. Rep. **7**, (2017).

<sup>42</sup> C.O. Avci, K. Garello, C. Nistor, S. Godey, B. Ballesteros, A. Mugarza, A. Barla, M. Valvidares, E. Pellegrin, A. Ghosh, I.M. Miron, O. Boulle, S. Auffret, G. Gaudin, and P. Gambardella, Phys. Rev. B - Condens. Matter Mater. Phys. **89**, (2014).

<sup>43</sup> Y. Ou, C.F. Pai, S. Shi, D.C. Ralph, and R.A. Buhrman, Phys. Rev. B **94**, 140414 (2016).

<sup>44</sup> Q. Shao, G. Yu, Y.W. Lan, Y. Shi, M.Y. Li, C. Zheng, X. Zhu, L.J. Li, P.K. Amiri, and K.L. Wang, Nano Lett. **16**, 7514 (2016).

<sup>45</sup> Z. Li, Z. Wang, Y. Liu, and W. Zhao, in *2018 IEEE 18th Int. Conf. Nanotechnol.* (IEEE, 2018), pp. 1–4.

<sup>46</sup> D. Zhu and W. Zhao, Phys. Rev. Appl. **13**, 044078 (2020).